Heat Treating Conference & Exposition, St. Louis, Missouri, on October 9 – 12, 2000

Computer Prediction and Evaluation of Inverse Quench-Hardening of Steel

K. Arimoto, D. Huang, D. Lambert, and W. T. Wu
Scientific Forming Technologies Corporation

Abstract

In oil quenched bearing grade steels, hardness distributions have occasionally exhibited lower hardness values at the surface than at the core. This phenomenon is referred to as "inverse quench-hardening". The Finite Element Method (FEM) system DEFORM™-HT was utilized to predict the volume fractions of metallic phases resulting from the inverse quench-hardening phenomenon. The simulated results have clarified the reasons for why the phenomenon occurs.

A COMPONENT having relatively small mass and high quenchability can be fully hardened to the center, while one with greater mass and lower quenchability may be hardened at the surface only. Cases have been reported however, where quenched steel components have exhibited higher hardness values at the core than the case. This phenomenon was labeled "inverse quench-hardening" by Shimizu and Tamura [1], since the resulting hardness characteristics appeared inverted when compared to the more conventional behavior, described above. The lower surface hardness was attributed to the transformation of pearlite [2], from simplified quenching experiments of cylindrical specimens made from a bearing steel. A theoretical explanation of the phenomenon was also proposed, using a CCT diagram, and considering discontinuous cooling rates [1,2,3].

Liscic et al [4,5] reported inverse quench-hardening phenomena in their Controllable Delayed Quenching (CDQ) technology polymer quench tests, involving AISI 4140 cylindrical specimens. Their explanation for the inverse hardening phenomenon was in direct agreement with that of Shimizu and Tamura [3].

The experiments carried out by Shimizu and Tamura [1,2] were simulated by the Finite Element Method (FEM) system DEFORM™-HT [6]. Volume fractions of the transformed phases were predicted by the code under the conditions for inverse quench-hardening to occur. The simulated results have explained that the phenomenon is related to a temperature recovery during quenching and that pearlite transformation occurs at the same time as latent heat is emitted.

Diffusion Type Transformation with Latent Heat

Before simulating the inverse quench-hardening phenomenon, the numerical model: DEFORM™-HT was verified. Previously simulated results by Agarwal et al [7] were used for this purpose.

Agarwal et al [7] studied the effects of latent heat on temperature and volume fraction changes in eutectoid carbon steel wire rods, during 20m/s forced air cooling. A TTT diagram for AISI 1080 carbon steel, containing 0.79%C and 0.76%Mn, was used for their calculations. The TTT diagram, an ASM publication [8], is shown in Fig. 1.

The heat transfer coefficient used in the calculations of Agarwal et al [7], did not appear to be clearly defined. The

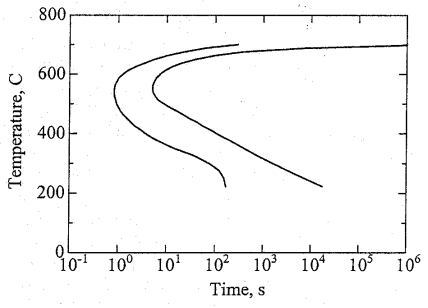

Fig. 1 - TTT diagram for AISI 1080 carbon steel

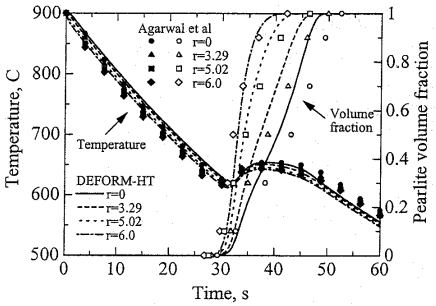

Fig. 2 - Temperature and pearlite volume fraction predictions in air-cooled cylinder (12mm dia.)

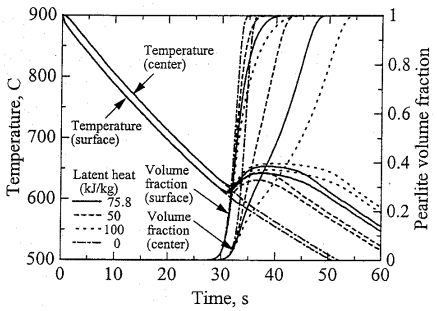

Fig. 3 - Temperature and pearlite volume fraction predictions using different latent heat values

authors reported that they used radiation theory and standard correlations for the cross flow of air over a cylinder; with an air-cooling velocity of 20 m/s.

During the current work, the heat transfer coefficient for cross flow of air over a cylinder was calculated using the following equation [9]:

$$Nu_f = cRe_f^m Pr_f^{0.37}(Pr_f / Pr_w)^{0.25} \quad (1)$$

where Nu , Re and Pr are the Nusselt, Reynolds and Prantdtl numbers, respectively. The subscripts f and w refer to the conditions of the main flow and the wall flow, respectively. Coefficients c and m were given the values: 0.26 and 0.6, respectively, for the validity condition: 1,000 < Re < 20,000. In the current work, a constant heat transfer coefficient value of 0.196 kW/m^{2}C was adopted, since it was a good approximation over the range of temperatures involved, and also because it easily facilitates further work. This constant value was calculated for the following conditions: cylinder diameter: 12mm, air flow velocity: 20 m/s, wall temperature: 500C and air flow temperature: 20C.

The thermal conductivity, specific heat and density for a eutectoid steel were referenced from available literature [10]. A latent heat of 75.8 kJ/kg was applied for the austenite-pearlite transformation. This was the value proposed by Kramer et al [11], and used previously by Agarwal et al [7].

Fig. 2 shows changes in temperature and pearlite volume fraction with time, from simulations by Agarwal et al [7] and DEFORM™-HT. In both cases, the cylinder was modeled as axisymmetric; in the current work, 50 uniform elements were applied across the radial direction. It is not clear however, how many radial elements were used by Agarwal et al [7], but the results compare very favorably.

The temperature difference between the center and surface of the cylinder is relatively small as shown by the radial symbols: r = 0.0 and r = 6.0 in Fig. 2. However, the local phase transformation at any given time is seen to vary more considerably throughout the cylinder and ultimately, the center transformation can be seen to take almost 10s longer than that at the surface. Agarwal et al [7] reported this observation but did not offer an explanation.

Three almost identical simulations were additionally carried out to study the effects of latent heat; three latent heat values of 0, 50 and 100 kJ/kg were applied. The results shown in Fig. 3 highlight that latent heat has an important influence on temperature and volume fraction changes during a quench simulation. The greater latent heat gives a longer time of transformation at the center, and vice versa. The case where latent heat = 0 showed no induced delay.

TTT Diagram and Volume Fraction Rate

To understand the different center and surface pearlite transformation characteristics, TTT diagrams and transformation kinetics were examined.

The experimental kinetics data were fitted using the following law developed by Johnson and Mehl [12]:

$$\xi = 1 - \exp(-bt^n) \quad (2)$$

where ξ is the phase volume fraction transformed, t is the time, and b and n are material constants defining the transformation data.

The b and n constants can be calculated from [6]:

$$n = \frac{\log\left\{\ln(1-\xi_f)/\ln(1-\xi_{ss})\right\}}{\log(t_f/t_s)} \quad (3)$$

$$b = \frac{1}{t_s^n}\ln\frac{1}{1-\xi_s} \quad (4)$$

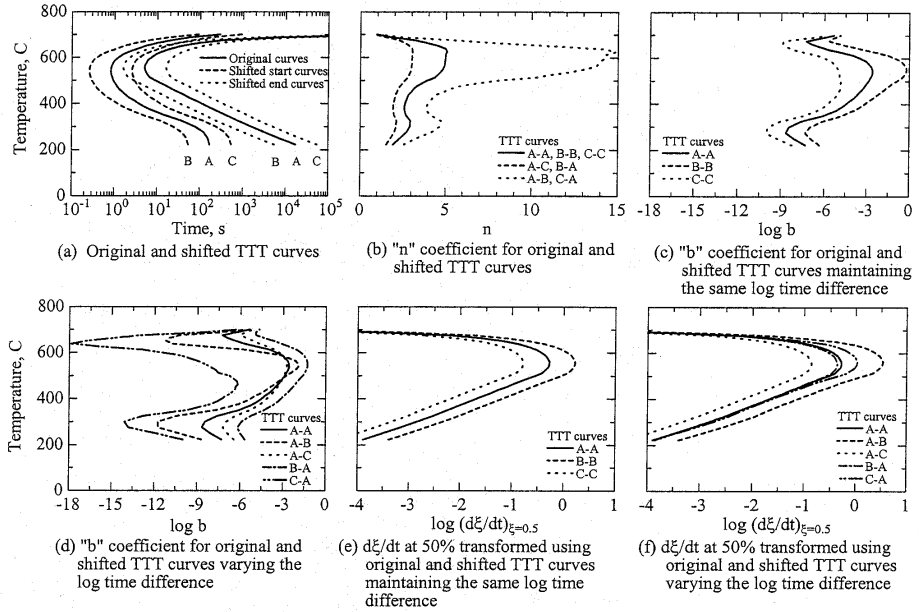

(a) Original and shifted TTT curves

(b) "n" coefficient for original and shifted TTT curves

(c) "b" coefficient for original and shifted TTT curves maintaining the same log time difference

(d) "b" coefficient for original and shifted TTT curves varying the log time difference

(e) dξ/dt at 50% transformed using original and shifted TTT curves maintaining the same log time difference

(f) dξ/dt at 50% transformed using original and shifted TTT curves varying the log time difference

Fig. 4 - Properties of original and shifted TTT curves from AISI 1080 steel

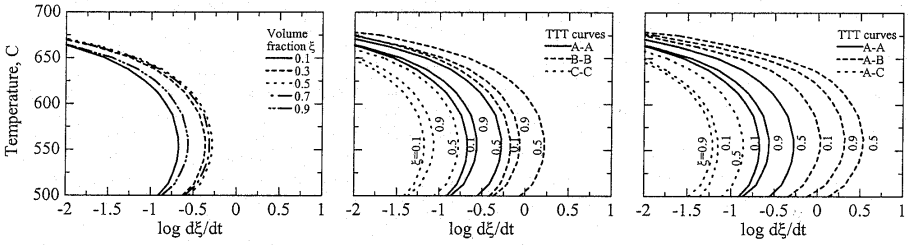

(a) Original TTT

(b) Original and shifted TTT curves maintaining the same log time difference

(c) Original and shifted TTT curves varying the log time difference

Fig. 5 - Volume fraction rate of original and shifted TTT curves from AISI 1080 steel

where ξ_s and ξ_f are the volume fractions of the TTT starting and finishing curves respectively. Times: t_s and t_f e the starting and finishing times of the TTT curve, respectively.

The volume fraction rate is useful to evaluate how active the transformation is at a given time. The time independent expression is derived from Eq.(2) as follows [6],

$$\frac{d\xi}{dt} = -\exp(-bt^n)\cdot(-bnt^{n-1})$$
$$= b^{\frac{1}{n}} n(1-\xi)\left|-\ln(1-\xi)\right|^{\frac{n-1}{n}} \quad (5)$$

The original TTT curves for the AISI 1080 steel shown in Fig. 1 were modified as illustrated in Fig. 4 (a) for examining the influence of TTT curve shifting on the

properties: n, b and $d\xi/dt$. The original starting and finishing TTT curves (labeled "A") were shifted in logarithmic time by -0.5 (labeled "B") and +0.5 (labeled "C"). In the current study, a given diagram's starting and finishing curves are distinguished by two labels; a TTT diagram may have A-A labels for the original curves and for example, A-B labels for an original starting curve and a modified finishing curve.

Temperature dependency curves of the n coefficients (from Eq. (3)) for the B-B and C-C curves, agreed with one of the A-A types, as shown in Fig. 4 (b). This suggests that the n coefficient remains constant if the logarithmic time difference between the shifted curves is the same as that between the original curves. A smaller logarithmic time difference produces a larger n value and vice versa, as compared to the original curves and is shown in Fig. 4 (b).

Figure 4 (c) and (d) illustrate temperature dependency curves of b coefficient (from Eq. (4)) for the original and shifted TTT curves. Unlike the n coefficient discussed above, it would appear that any shifting of either a starting or finishing TTT curve would yield a change in the b coefficient curve.

Temperature dependency curves of the volume fraction rate at $\xi = 0.5$, i.e., $(d\xi/dt)_{\xi=0.5}$, were plotted from Eq. (5) as shown in Fig. 4(e) and (f). Figure 4 (e) shows that a left shift of the starting and finishing TTT curves (maintaining the same logarithmic time difference), produced a larger volume fraction rate than originally, and a right shift gave the opposite. Shifting the curves to the left and decreasing the logarithmic time difference generally resulted in a greater volume fraction rate than the original, whereas shifting to the right and increasing it gave a lesser rate.

Figure 5 shows the characteristics of volume fraction rate, $d\xi/dt$, to be dependent on not only the temperature but also phase volume fraction transformed. Curves of volume fraction rate calculated from the original TTT curves, as shown in Fig. 5 (a), exhibit a maximum at ξ=0.5. Consequently, such curves calculated at $\xi = 0.5$ may be extremely useful when comparing transformation rates in different steels.

The spacing between ξ=0.1, 0.5 and 0.9 curves did not change significantly when comparing the original and shifted B-B and C-C TTT curves (see Fig. 5 (b)). However, the spacing differed slightly when comparing the shifted TTT A-B and A-C results, as shown in Fig. 5 (c).

Prediction of Pearlite Transformation Using Shifted AISI 1080 TTT Diagrams

In order to investigate the effects of curve shifting on transformation delay, the TTT A-B and A-C curves were compared to the original A-A curves in three otherwise identical simulations of an AISI 1080 steel cylinder. The DEFORM™-HT predictions show a greater transformation

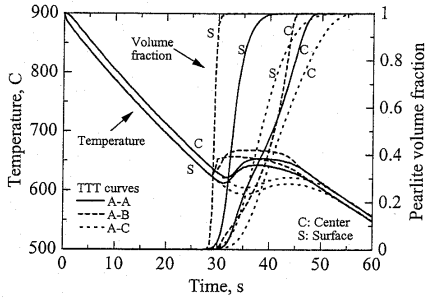

Fig. 6 - Temperature and pearlite volume fraction predictions for original and shifted TTT curves from AISI 1080 steel

delay at the center of the cylinder, using the A-B curves, as compared to the originals (shown in Fig. 6). However, less delay in the center (as compared to the originals) resulted from the A-C curves.

To examine the results in finer detail, time-history curves of temperature and volume fraction rate were plotted and are shown in Fig. 7. The curves were plotted over that part of a transformation where a latent heat would be induced. Results from the original A-A, shifted A-B and shifted A-C, are shown in Fig. 7 (a), (b) and (c) respectively. The circular symbols on each curve indicate the discrete volume fractions of 0.1 through 0.9 by an increment of 0.1. For clarity, the incremental values are shown for only one of the curves in each figure.

From the results (Fig. 7 (a) and (b)) it can be seen that the surface volume fraction rate, using the shifted A-B curves, reaches a higher peak more rapidly than when the original A-A curves were applied. In addition, over a time period from 40 to 45s, the center volume fraction rate calculated from the A-B characteristic is shown to be greater than with the original, A-A curves. Such a surface/center difference was not evident from the results of the A-C data, as shown in Fig. 7 (c).

Figure 8 shows locus curves of the volume fraction rates, calculated using the A-A, A-B and A-C TTT diagrams, where curves are plotted for both center and surface locations of the cylinder. Additional locus curves for the original A-A diagram were added to Fig. 8; these loci did not consider any latent heat. When a latent heat was not taken into account, the center and surface curves had almost the same shape and were almost superimposed on each other. This was not the case when latent heat was considered, as the resultant curves had very different shapes and were not close to each other on the temperature-volume fraction rate chart. Generally, when the center and surface curves are far apart from each other (Fig. 8), the transformation delay becomes significant.

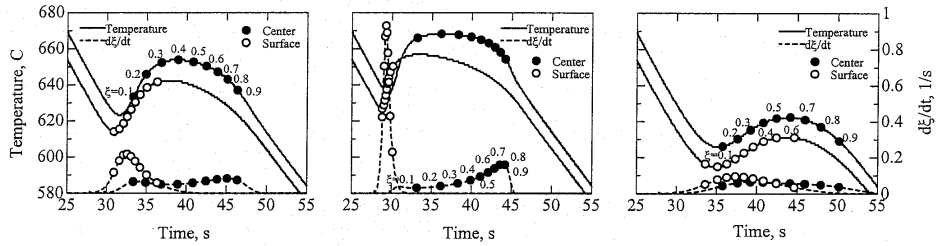

Fig. 7 - Temperature and pearlite volume fraction rate time histories at center and surface locations using original and shifted TTT curves from AISI 1080 steel

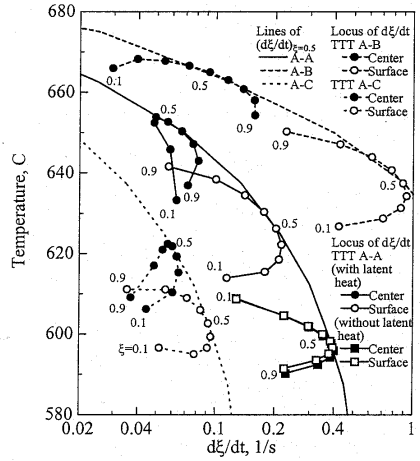

Fig. 8 - Loci of center and surface volume fraction rate from A-A, A-B and A-C TTT curves

Shimizu and Tamura's Experiments

Shimizu and Tamura [1,2] introduced a simplified experimental program using cylindrical specimens of a spheroidized SUJ2 steel (Japanese standard for bearing steel). The purpose was to analyze the components of the inverse quench-hardening phenomenon occurring under production conditions. The chemical compositions of the specimens were slightly different for each cylinder diameter, as shown in Table 1.

After austenitizing at 840C for 20 minutes, the specimens were initially cooled in air, then finally quenched in a 5% brine solution. Shimizu and Tamura [1,2] proposed that the inverse quench-hardening phenomenon occurring during oil quenching, was due to the formation of the vapor blanket. Air-cooling during the simplified experiments was intended to simulate the vapor blanket stage and allow greater control of the cooling rate.

Table 1 - Nominal compositions of the SUJ2 steel specimens

Specimens (Diameter x Length)	C	Si	Mn	Cr
10mm x 40mm	1.01	0.24	0.41	1.46
15mm x 40mm	0.97	0.25	0.42	1.46
20mm x 40mm	1.02	0.24	0.36	1.36
25mm x 50mm	0.95	0.27	0.37	1.37
30mm x 60mm	0.96	0.27	0.38	1.35
36mm x 80mm	0.97	0.26	0.40	1.39

Experimental results reported by Shimizu and Tamura [1,2] consisted of measured hardness distributions and micrographs of specimens' microstructures; there was an absence of any published cooling curve results from the quenching experiments. The specimens' measured Rockwell C hardness distributions are shown in Fig. 9, where the time shown adjacent to each curve indicates the period of air-cooling. The distributions show the inverse quench-hardening phenomenon over a certain period of air-cooling duration. The results clearly illustrate that both the duration of air-cooling and cylinder diameter have an effect on the resultant hardness distribution.

Shimizu and Tamura [1,2] performed metallography on the quenched specimens, in particular, electron microscopy of replicas. Their observations highlighted the existence of coarse pearlite with a small amount of fine pearlite, surrounded by martensite. This particular microstructural feature was evident in the location where inverse quench-hardening had occurred.

Shimizu and Tamura [1,2] also investigated the metallic structure of a commercial grade steel bearing race, which had exhibited the inverse quench-hardening phenomena after oil quenching. Fine pearlite was observed during electron microscopy investigations on their replicas. In addition, it was reported that fine pearlite tended to be

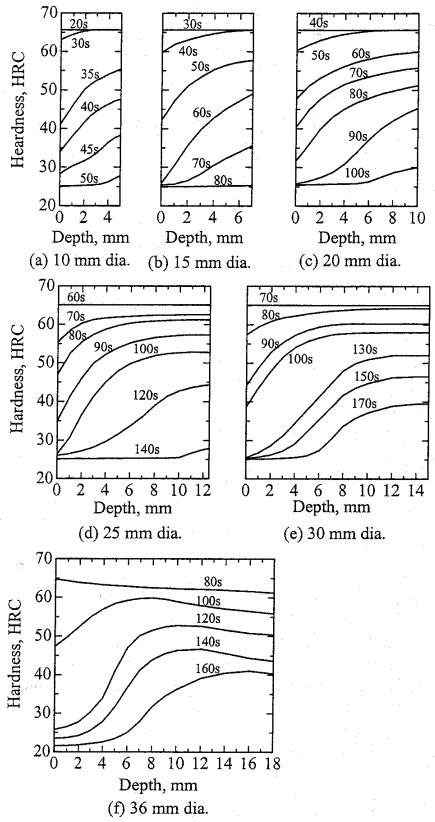

Fig. 9 - Hardness distribution in specimens of various diameters quenched into 5% brine after air cooling for various periods

induced by cooling rates greater than those involved in air cooling.

Shimizu [2] offered an explanation for the inverse quench-hardening phenomenon based on findings in a 20mm diameter specimen. The specimen had been cooled for 50 seconds in air, followed by a brine quench; a modified CCT diagram was used, which considered different cooling rates [2]. The explanation described how fine pearlite was transformed during the brine quench as opposed to the air-cool. However, pearlite was observed with a small amount of fine pearlite in the area corresponding to the inverse quench-hardening phenomena.

Prediction of Inverse Quench-Hardening Phenomenon

The experiments of Shimizu and Tamura [1,2] which exhibited the inverse quench-hardening phenomenon, were simulated by DEFORM™-HT. Since Shimizu [2] only provided a TTT starting curve for the SUJ2 alloy, the current work has utilized the TTT curves of three bearing steels, similar in composition, 52100 [8], En 31 [13] and 100 Cr 6 [14]. The above TTT diagrams are shown in Fig. 10 (a) with the starting curve from Shimizu [2]. The chemical compositions of the 52100, En 31 and 100 Cr 6 steels used can be found in Table 2.

As the TTT curves from the various sources were drawn using different starting and finishing volume fractions, the curves have been normalized for starting and finishing conditions of: ξ_s=0.1% and ξ_f=99.9% as shown in Fig. 10 (b). After the conversion, the TTT curves of each of the steels were more comparable.

The volume fraction rates of each steel at 50% transformed are shown in Fig. 10 (e) and were found to agree reasonably well with each other. In contrast, the coefficients *n* and *b* shown in Fig. 10 (c) and (d) exhibited greater differences.

The carbon steel latent heat value of 75.8 kJ/kg [11] was used in the current work simulations. Figure 11 shows the separate heat transfer coefficients used for the air cooling and 5% brine quenching. The air-cooling value was estimated from the cooling curves measured in steel cylinders by Scott [15]. The coefficient for the 5% brine solution was calculated using the lumped-heat-capacity method [16], from a cooling curve obtained by the JIS silver probe.

The 20mm diameter cylinder was simulated by DEFORM™-HT, using TTT diagrams for three different alloys: 52100, En 31 and 100 Cr 6. The time histories of temperature and phase volume fraction are shown in Fig. 12, for both center and surface locations of the specimen. Although each TTT diagram was measured from an alloy similar to the SUJ2 grade, the results showed differences. The results from the 52100 and En 31 alloys show a significant transformation delay at the center, in contrast to that of the 100 Cr 6.

Table 2 - Nominal compositions of the bearing steels from which TTT was created

Steel	C	Si	Mn	S	P	Cu	Ni	Cr	Mo	V	Grain size	Austenized temp.
52100	1.02		0.36				0.20	1.41			9	843C
En31	1.08	0.25	0.53	0.015	0.022		0.33	1.46	0.06		7	820C(for 30min)
100 Cr 6	1.04	0.26	0.33	0.006	0.023	0.20	0.31	1.53	<0.01	0.01		860C

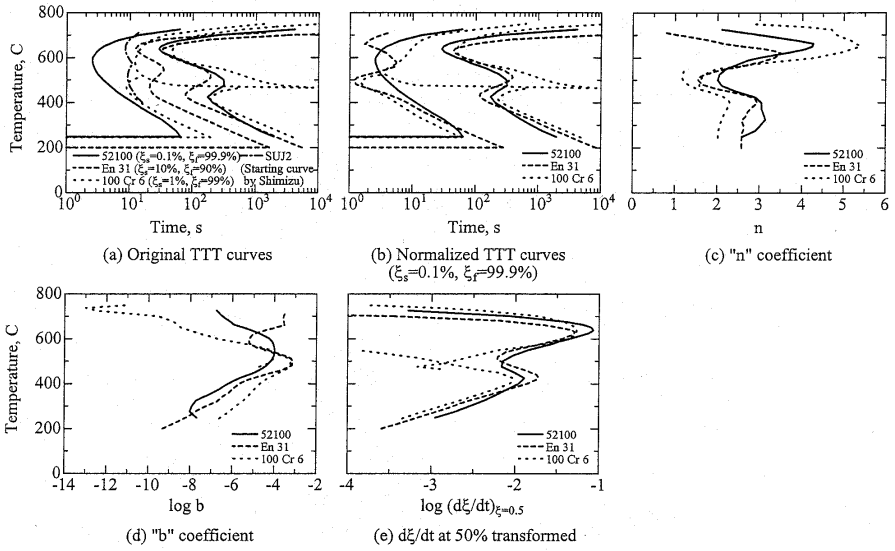

(a) Original TTT curves (b) Normalized TTT curves (ξ_s=0.1%, ξ_f=99.9%) (c) "n" coefficient

(d) "b" coefficient (e) dξ/dt at 50% transformed

Fig. 10 - Properties of TTT curves of three bearing steels

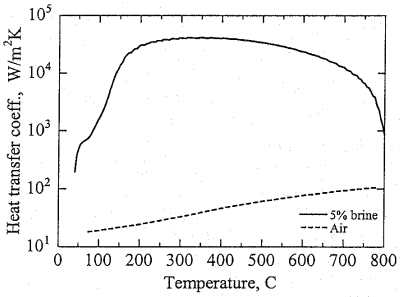

Fig. 11 - Heat transfer coefficients for air cooling and 5% brine quenching

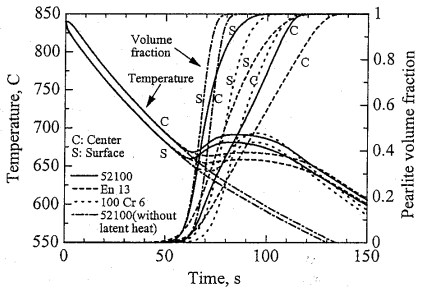

Fig. 12 - Temperature and pearlite volume fraction predictions from three different bearing steel TTT curves in a 20 mm dia. cylinder

Figure 12 includes the 52100 TTT results simulated academically without accounting for latent heat. The temperatures at both surface and center locations are continuously cooling and at no time is there an increase in temperature due to latent heat. The surface and center volume fraction curves are parallel for the entire transformation period, hence there is no delay induced in contrast to when latent heat is accounted for.

In addition, the time histories of temperature and volume fraction rate for three bearing steels are plotted in Fig. 13. This plot spans a duration in the transformation when a latent heat is induced. The circular symbols on each curve indicate the discrete volume fractions of 0.1 through 0.9 by an increment of 0.1. For clarity, the incremental values are shown for only one of the curves in each figure.

The surface volume fraction rate from the 52100 TTT data exhibited a higher peak than that from the En 31 alloy. This is shown in Fig.13 (a) and (b). The activating period of the 52100 result is shorter than that of the En 31 result. This is true for both center and surface locations. The 100 Cr 6

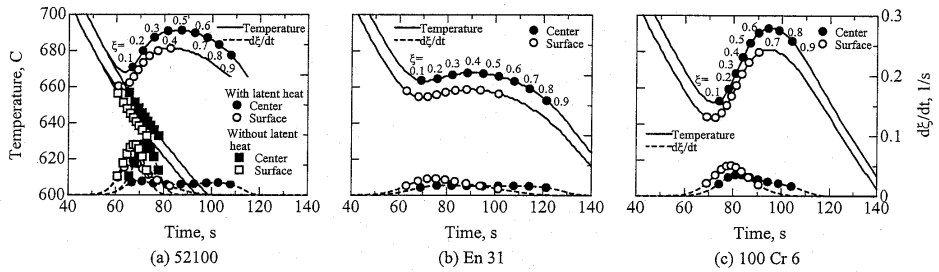

Fig. 13 - Temperature and volume fraction rate time histories at center and surface locations in a 20 mm dia. cylinder using three different bearing steel TTT curves

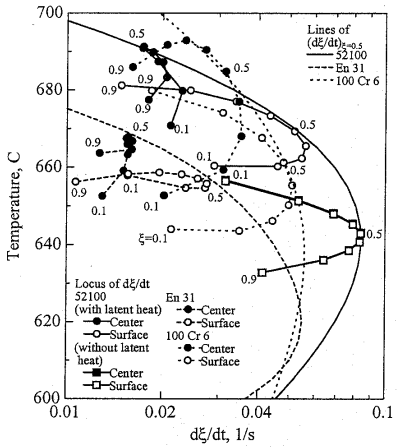

Fig. 14 - Loci of center and surface volume fraction rate in a 20 mm dia. cylinder using three different bearing steel TTT curves

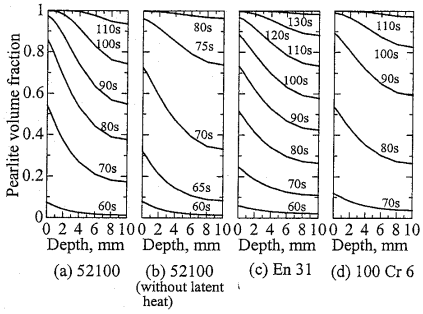

Fig. 15 - Pearlite volume fraction predictions in a 20 mm dia. cylinder for three different bearing steels

volume fraction rate shows a very similar trend at the center and surface and is shown in Fig. 13 (c).

The 52100 alloy was also used to highlight the effect of accounting for latent heat in a simulation. Fig. 13 (a) illustrates that for the center location, the activating period is less when latent heat is ignored. The curves of surface volume fraction rate, both when accounting for and ignoring latent heat, are practically superimposed upon each other.

Surface and center volume fraction rate loci, are shown in Fig. 14. The rate curves are shown for all 3 bearing steel TTT data. The locus curves from the 100 Cr 6 alloy data have a very different pattern as compared to the 52100 and En 31 steels. This difference may be related to the different curvature of the 50 % transformed volume fraction rate curves. The reason why the transformation from the 52100 TTT curve is more active than from the En 31 data, is illustrated by the different locations of locus curves between the two alloy results. Generally, a more active transformation is achieved when a locus which is located further to the right side.

The locus curves from the 52100 alloy ignoring latent heat are also shown in Fig. 14, where they are shown to be located in a lower temperature range than those accounting for latent heat. Also, the surface and center curves are practically superimposed upon each other, indicating a lack of transformation delay.

Figure 15 shows four distributions of pearlite volume fraction in a 20mm diameter cylinder, simulated using the three bearing steels' TTT data. The time shown adjacent to each curve indicates the period of air-cooling. The shapes of distributions are similar to one another, however, there appears to be a discrepancy in the timings. The time dependency of the volume fraction curves from the 52100 alloy (Fig. 15 (a) and (b)) shows that the more rapid transformation was found, ignoring latent heat.

Since a brine quench has high quenchability, the austenite present in a specimen after air-cooling would be almost completely transformed to martensite during brine quenching. Therefore, the inverse quench-hardening phenomenon is very likely in a specimen where pearlite has transformed on and near to the surface, during the air cool period.

Predicted time histories of temperature and volume fraction, as a function of cylinder diameter, are shown in Fig. 16, from the 52100 data. Larger diameter specimens induced greater transformation delays in the center.

Simulations incorporating both air and brine cooling were carried out to establish the quenchability of brine. Figure 17 shows the time histories of temperature and volume fraction in the 20mm diameter cylinder from 52100 data. Five different times for air cooling were investigated: 60, 70, 80, 90 and 100 seconds, followed by the 5 % brine quench. Once the brine quenching started, the pearlite transformation at the surface is suddenly stopped. The transformation at the center continues for a few seconds longer.

The experimental and predicted hardness distributions in the 20 and 36mm diameter cylinders were compared as shown in Fig.18. The simulated volume fractions of pearlite and martensite were used to estimate the hardness values. Working from phase hardness values of 25 and 66 HRC, for pearlite and martensite respectively, a simplified mixture rule established the resultant hardness distributions

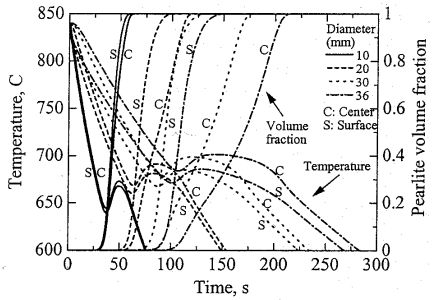

Fig. 16 - Temperature and pearlite volume fraction predictions at center and surface locations in cylinders of various diameters using 52100 TTT curves

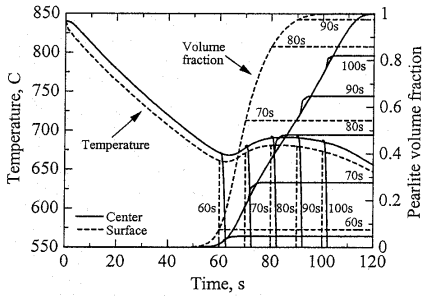

Fig. 17 - Temperature and pearlite volume fraction predictions at center and surface locations in a 52100 bearing steel cylinder (20mm dia.) for both air cooling and 5% brine quenching

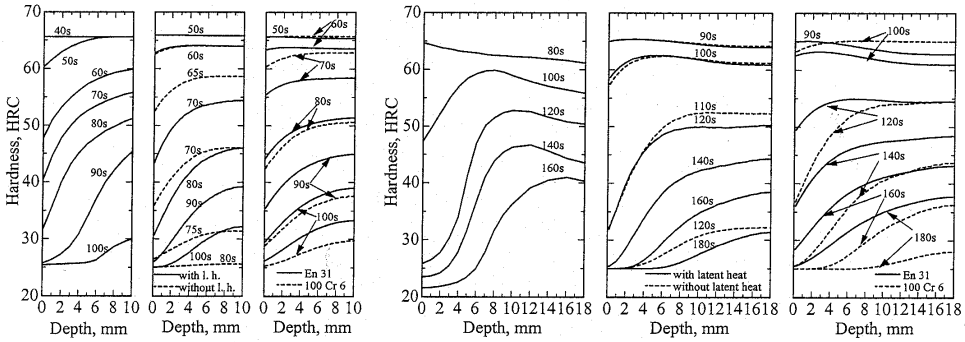

Fig. 18 - Experimental and simulated hardness distribution in bearing steel cylinders quenched by 5% brine after air cooling of various periods

in the specimens.

The hardness predictions have similar shaped characteristics to the experimental results of Simizu and Tamura [1,2], that is, they all indicate inverse hardening. However, there were discrepancies in the hardness magnitudes and timings.

As for the 20mm diameter cylinder (shown in Fig. 18 (a)), inverse quench-hardening phenomena were observed in experimental specimens, quenched into brine after 50 to 100s of air-cooling. However, the corresponding simulations which accounted for latent heat, exhibited the inverse quench hardening phenomena after the slightly later periods of 60 to 100 seconds of air cooling. In addition, the same simulations using 52100 data, without accounting for latent heat showed the phenomena occurring after 60 to 80 second time periods.

Hardness results for the 36mm diameter cylinder (Fig. 18 (b)) show similar discrepancies between experiment and prediction as the 20mm diameter specimens. For the quench simulations involving the 100, 120 and 140s air-cooling periods, the predictions did not show as much softening at the core, as compared to measurement.

One reason for the discrepancy could be due to the non-availability of TTT data for Simizu and Tamura's [1,2] steel specimens. It is believed that the process is extremely sensitive to minor differences in TTT data. In addition, the value of latent heat used in the simulations was established from a eutectic carbon steel and therefore may not have been completely suitable for the bearing steels analyzed in the current work. The existence of cooling curves during quenching would help to verify simulated results.

Conclusions

The inverse quench-hardening phenomena in bearing steel specimens, initially cooled in air and then quenched in 5% brine, was simulated by DEFORM™-HT and compared with experimental results. Obtained conclusions are summarized as follows:

(1) The hardness distributions predicted from volume fractions of pearlite and martensite, exhibited the inverse quench-hardening characteristic. There was however, a discrepancy in the hardness magnitudes from the different air cooling times.
(2) Pearlite transformation was predicted during air-cooling as opposed to brine quenching, which was described in previous work, involving a graphical method in which latent heat could not be considered.
(3) Predictions highlighted that pearlite volume fraction rate characteristics are significantly influenced by the amount of latent heat and differences in TTT data.
(4) It was found that the locus curves of volume fraction rate are extremely valuable for comparing the characteristics of transformation in different alloys.

In order to gain a more complete understanding of the inverse quench-hardening phenomena, it is suggested that work ought to concentrate on:

(1) Further cooling curve measurements and more precise TTT and latent heat data for the alloys used in the current work.
(2) Further experiments and computer simulations on the practical inverse quench-hardening phenomena which occur in production quench processes.

The authors express their gratitude to Professor M. Narazaki, Utsunomiya University, for providing a heat transfer coefficient of brine quenching.

Reference

1 N. Shimizu and I. Tamura, Trans. ISIJ, 16, 655-663 (1976)
2 N. Shimizu, doctoral thesis for Kyoto University (1985) (in Japanese)
3 N. Shimizu and I. Tamura, Trans. ISIJ, 17, 469-476 (1977)
4 B. Liscic, V. Grubisic and G. E. Totten, Proc. 2nd Intl. Conf. Quenching and Control of Distortion, Cleveland, 47-54 (1996)
5 B. Liscic and G. E. Totten, Advanced Materials & Processes, 9, 180-184 (1997)
6 K. Arimoto, G. Li, A. Arvind, and W. T. Wu, Proceedings of the 18th ASM Heat Treating Society Conference & Exposition, 639-644 (1998)
7 P. K. Agarwal and J. K. Brimacombe, Metall. Trans., 12B, 121-133 (1981)
8 "Atlas of Time-Temperature Diagrams for Irons and Steels", ASM (1991)
9 A. Zukauskas, Advances in Heat Transfer, 8, 93-160 (1972)
10 "Physical Constants of Some Commercial Steels at Elevated Temperature", edited by British Iron and Steel Research Association, Butterworths Scientific Publications (1953)
11 J. K. Kramer, G. M. Pound, and R. F. Mehl, Acta Metall., 6, 653-771 (1958)
12 W. A. Johnson and R. H. Mehl, Trans. AIME, 135, 416-458 (1939)
13 "Atlas of Isothermal Transformation Diagrams of B.S. En Steels", 2nd edition, submitted by British Iron and Steel Research Association, Special Report No. 56, The Iron and Steel Institute, London (1956)
14 "Atlas zur Warmebehandlung der Stahle", vol 1, Max-Planck-Institut fur Eisenforschung, Verlag Stahleisen mbH, Dusseldorf, Germany (1954)
15 H. Scott, Trans. ASM, 22, 577-604 (1934)
16 M. Narazaki and E. Y. Ju, Proc. 18th ASM Heat Treating Conference, ASM International, 629-638 (1998)